
Weight-Aware Implicit Geometry Reconstruction with Curvature-Guided Sampling

Lu Sang Abhishek Saroha Maolin Gao Daniel Cremers

Computer Vision Group

Technical University of Munich

lu.sang, abhishek.saroha, maolin.gao, cremers@tum.de

Abstract

Neural surface implicit representations offer numerous advantages, including the ability to easily modify topology and surface resolution. However, reconstructing implicit geometry representation with only limited known data is challenging. In this paper, we present an approach that effectively interpolates and extrapolates within training points, generating additional training data to reconstruct a surface with superior qualitative and quantitative results. We also introduce a technique that efficiently calculates differentiable geometric properties, i.e., mean and Gaussian curvatures, to enhance the sampling process during training. Additionally, we propose a weight-aware implicit neural representation that not only streamlines surface extraction but also extend to non-closed surfaces by depicting non-closed areas as locally degenerated patches, thereby mitigating the drawbacks of the previous assumption in implicit neural representations.

1 Introduction

3D reconstruction, vital in fields like computer graphics, robotics, and computer vision, creates three-dimensional models from various data sources. Visualization typically involves either explicit or implicit surface representations. Explicit methods offer direct 3D model information but struggle with complex topologies, resolution adjustments, and local modifications, while implicit representations, such as signed distance function (SDF), address these issues but have high memory demands. Nowadays, neural implicit functions retain the advantages of implicit representation while solving storage problems and breaking the barrier of resolutions. In many real-world applications, often only point clouds with limited density are available for training a neural network to approximate the neural implicit representation of a surface. Additionally, traditional neural implicit representation is limited to closed surfaces, as it requires well-defined inside and outside regions. To address these challenges, in this paper, we present a sampling method that effectively interpolates and extrapolates within training data, leading to more accurate and robust results. Furthermore, the proposed method samples point in a curvature-guided manner and present a technique for computing differentiable geometric curvature without relying on a mesh, which aids in point sampling during training and overcomes the uneven sampling problem. We further propose a weight-aware implicit neural representation capable of representing non-closed areas, expanding the applicability of our method to a broader range of surface types. In summary, we propose the following contributions:

- We introduce an approach that can effectively handle depth or point cloud input for precise implicit learning by efficiently interpolating and extrapolating the input data.
- We develop a method that seamlessly incorporates curvature information from inputs, aiding in point sampling during training.
- We put forth a weight-aware implicit neural representation that is capable of representing non-closed surfaces by treating non-closed areas as locally degenerated surfaces.

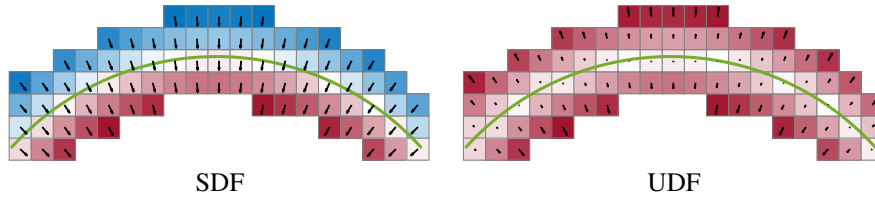


Figure 1: Gradient analysis of two types of the distance function of a circle. In SDF (left), the gradient of SDF is well-defined everywhere. In UDF (right), the sign is all same inside or outside of the iso-surface, whereas USD has a noisy numerical gradient at the surface, which is a direct consequence of its non-differentiability, hence jeopardizing shape reconstruction quality.

2 Related Work

2.1 Surface Representation

Surface representation can be classified into two categories based on the stored surface properties: explicit surface representation (e.g., polygon mesh or point clouds) and implicit surface representation (e.g., signed distance field). Further, based on the storage method for surface properties, it can also be divided into classical surface representation and neural network-based methods. Classical methods discretize the space explicitly, storing individual properties of each discrete part, such as voxels or triangle meshes. In contrast, network-based methods utilize a neural network to store surface properties. On the other hand, implicit neural representation brings numerous benefits, addressing many of the limitations of explicit methods. There are two types of implicit functions for surface representations.

Signed Distance Field The signed distance function (SDF) stores the shortest distance of a given point to a surface, with the sign indicating whether the point is inside or outside the surface. It Offers numerous advantages for surface representation, such as smooth interpolation between shapes or poses, making it suitable for shape morphing, character animation, and blending [26; 11]. Geometrically, SDF gradients provide normal vectors, helpful in locating surface points, shading, physics simulations, and geometric processing [24; 22]. However, SDF is designed for closed surfaces, requiring well-defined "inside" and "outside" notions, which may hinder performance when representing large, typically unclosed, scenes.

Unsigned Distance Field To address the limitations of SDFs, NDF [4] proposed using an Unsigned Distance Field (UDF) to circumvent the need to distinguish between the inside and outside of surfaces. This approach offers several advantages, such as reconstructing open surfaces and computing ground truth distances while sampling in space using nearest neighbor search. However, losing sign information introduces ambiguity in surface reconstruction, such as correct surface orientation and normal direction. Additionally, UDF is less efficient in space partitioning and zero-isosurface finding. While UDF is differentiable in most areas, it is not differentiable at surface points, which are the most critical. Consequently, surface normals cannot be computed for points on the surface.

2.2 Neural Implicit Surface Representation

Implicit Function Learning (IFL) employs learning-based methods to train a neural network that represents surfaces using occupancies [14; 9; 3], signed [18; 11; 17; 2; 15], or unsigned distance functions [4]. The primary advantage of neural implicit surface representation lies in encoding surface properties, such as distance and occupancies, within a neural network, rather than explicitly storing them for each surface point. As a result, one can query any 3D points in space to obtain the corresponding attributes. This approach allows for the recovery of highly detailed surfaces at a lower memory cost compared to traditional surface representation methods such as classical SDF or NDF. Moreover, it is a continuous representation suitable for further mathematical analysis of the represented surface.

2.3 Points Sampling in Implicit Function Learning

Numerous studies have proposed methods to address the problem of recovering surface mesh from given point clouds using IFL [23; 4; 9; 17]. The general approach entails iteratively sampling points in conjunction with the desired ground truth properties in the space for training data and utilizing the known ground truth values to supervise network training. For instance, [17] employs mesh as input and computes the SDF of sampling points as input data for training. The works of [4; 3] voxelized a

mesh, calculated the occupancy of the voxel, and then used the voxel as training data input. However, a drawback of these approaches is that the network structure must conform to the preprocessed voxel grid resolution.

Sampling from point cloud However, the ground truth mesh of an object is not always available in practice. When only a point cloud is available, obtaining ground truth distances when sampling outside of the point cloud points is challenging. Consequently, the sampling is limited to random sampling in point cloud points. Therefore the training domain is finite, while the inference domain is typically more significant than the training domain. Moreover, many works also require known normals for surface points to achieve satisfactory results which may not always be readily available.

Biased sampling Another problem of uniform sampling is, as discussed by [26] and [17], the naive uniform sampling on the surface points for limited iterations result in biased samples. To avoid this issue, [26] samples not only on the surface but also near the iso-surface with some tolerance. However, choosing a suitable tolerance threshold often requires object-dependent hyperparameter tuning.

This paper presents a method that starts with depth images or point clouds to initialize a coarse voxel grid, along with SDF values, normals, and curvature information for subsequent training. Our approach leverages a hybrid representation, combining point clouds and voxels, to facilitate easy extrapolation and interpolation of sampling within the initial data, ultimately improving ILF accuracy. Additionally, our sampling method incorporates curvature to mitigate biased sampling effects. Overall, our technique expands the range of applications and makes acquiring training data more practical.

3 Reconstruct Surface via Implicit Neural Field

Due to the numerous benefits of implicit neural representation, many works attempt to recover the neural signed distance field of a surface. In general, the problem is stated as follows: Given noisy measurements of a continuous surface $\mathcal{S} \subset \mathbb{R}^3$ as input, e.g., a point cloud $\mathcal{P} = \{\mathbf{x}_i\}$, for $\mathbf{x}_i \in \mathbb{R}^3$, $i \in \mathcal{V}$, where \mathcal{V} is the index set. The goal is to estimate the (signed) distance field of the surface, which is parameterized by a neural network $f(\mathbf{x}; \theta) : \mathbb{R}^3 \rightarrow \mathbb{R}_+$ (or \mathbb{R}) with the learnable parameter θ and query point $\mathbf{x} \in \mathbb{R}^3$. The conventional approach to recovering the implicit function involves minimizing

$$l(\theta) = l_{\mathcal{X}}(\theta) + \tau_n l_{\mathcal{N}}(\theta) + \tau_e l_{\mathcal{E}}(\theta), \quad (1)$$

where $l_{\mathcal{X}}(\theta)$ is the geometric constraint on the surface, $l_{\mathcal{N}}(\theta)$ is the (optional) normal constraint when normal information is available. The term $l_{\mathcal{E}}(\theta) = \mathbb{E}_{\mathbf{x}}(\|\nabla_{\mathbf{x}}f(\mathbf{x}, \theta) - 1\|^2)$ is called Eikonal constraint, $\tau_n \geq 0$, $\tau_e \geq 0$ are the weights of normal term and Eikonal term.

Signed Distance Field Learning via Point Clouds Point clouds are commonly used as practical input in many studies to recover the neural representation of a surface, i.e. $\mathcal{P} = \{\mathbf{x}_i\}, i \in \mathcal{V}$. Then the geometry constraint in equation (1) is $l_{\mathcal{X}}(\theta) = \frac{1}{|\mathcal{V}|} \sum_{i \in \mathcal{V}} |f(\mathbf{x}_i, \theta)|$ [11; 23], as input points lie on the surface, making the distance to the closest surface zero. In addition, when point cloud normals are known, using point-normal pairs $\{\mathbf{x}_i, \mathbf{n}_i\}, i \in \mathcal{V}$ as input allows the normal constraint to be computed as, for instance, $l_{\mathcal{N}}(\theta) = \frac{1}{|\mathcal{V}|} \sum_{i \in \mathcal{V}} \|\nabla_{\mathbf{x}}f(\mathbf{x}_i, \theta) - \mathbf{n}_i\|$, minimizing normal alignment error [11]. However, this approach has drawbacks. Point clouds only contain limited input information, and for a randomly sampled point cloud, it isn't easy to reconstruct the underlying continuous surface. As a result, IFL methods typically only sample within the given point cloud for training [11; 9; 23], hindering the training convergence and leading to unsatisfying reconstruction quality (see section 6 for discussions). Consequently, many studies prefer to use meshes as input for training data sampling [4; 26], but obtaining meshes can be challenging in real-world applications.

4 Curvature-Guided Sampling and Unclosed Surface Representation

With the previously mentioned constraints in mind, to reconstruct target surface \mathcal{S} , we propose the gradient-SDF method [24] to derive a voxelized point cloud. This approach offers practical and theoretical benefits. It retains the continuous surface representation theoretically, enabling more efficient point sampling and interpolation in space. On a practical level, the method allows precise normals acquisition from a depth-derived voxel volume [24] and facilitates easy curvature calculation, further discussed in section 4.2. Unlike earlier studies [4; 3] that required network adaptation to

the voxelized input mesh, our approach maintains point cloud structure irrespective of voxelization resolution. In essence, our hybrid method combines the merits of point cloud and voxel shape representation, enhancing reconstruction results as demonstrated in section 6.

4.1 Voxel Utilization and Sampling

We utilize the initial voxel grid $\{\mathbf{v}_i\} \subset \mathbb{R}^3$ contain SDF value for each voxel following the method described in [24] if depth images are available. For each voxel $\mathbf{v} \in \mathbb{R}^3$, (we drop the sub-index i for simplification) the following properties are initialized: its SDF value $\psi^v \in \mathbb{R}$, distance gradient $\mathbf{g}^v \in \mathbb{R}^3$, and weight of SDF value $w^v \in [0, 1]$. The voxel weight measures the reliability of the information stored in the voxel, with 1 indicating the highest and 0 the lowest reliability respectively. For detailed formulation, please refer to [24]. Given a point $\mathbf{x} \in \mathbb{R}^3$ in 3D space, we can localize which voxel the point \mathbf{x} lays in and denote that voxel as $\mathbf{v}(\mathbf{x})$, then we can obtain the signed distance value using Taylor expansion with the help of stored distance gradient

$$\psi^x = \psi^v + \langle \hat{\mathbf{g}}^v, \mathbf{x} - \mathbf{v}(\mathbf{x}) \rangle, \quad (2)$$

where $\hat{\mathbf{g}}^v = \frac{\mathbf{g}^v}{\|\mathbf{g}^v\|}$ is the normalized gradient of the distance field. Meanwhile, the point \mathbf{x} inherits the weight of its voxel w^v . Thus, we can sample any point in the space for training, and our sampling method does not require any additional nearest neighbor search and is free from the voxel resolution, since the input sample for the training is points-signed distance value pair. Moreover, point cloud points that are encoded in a voxel grid can be retrieved by

$$\mathbf{x} = \mathbf{v}(\mathbf{x}) - \psi^v \hat{\mathbf{g}}^v. \quad (3)$$

Plug equation (3) to (2), then we get the SDF value

$$0 = \psi^v + \langle \hat{\mathbf{g}}^v, -\psi^v \hat{\mathbf{g}}^v \rangle, \quad (4)$$

since $\hat{\mathbf{g}}^v$ is a unit vector. Thus \mathbf{x} lays on the iso-surface. Due to the fact that the surface normal \mathbf{n} coincides with the normalized gradient, thus we naturally have the points-normal pair $\{\mathbf{x}, \hat{\mathbf{g}}^v\}$. The equation (2) allows us to interpolate inside voxels and also extrapolate in any 3D point in the sample domain together with the weight.

4.2 Curvature Computation

Yang et al. [26] and Novello et al. [17] point out that uniformly sampling on the surface points especially using the equation (3) results in points gathering high-curvature area. To avoid this problem, Yang et al. [26] samples within a band near the iso-surface $\{\mathbf{x} \in \Gamma | \psi < \gamma\}$, where Γ is the sample domain and $\gamma > 0$ is the SDF threshold. Novello et al. [17] use mesh inputs to compute principal curvature information, dividing points into low, medium, and high curvature categories according to the absolute sum of two principal curvature κ_1 and κ_2 . However, this process cannot be done without a mesh. To use a more scale invariant sampling strategy without mesh, we consider using differential geometry properties such as mean curvature and Gaussian curvature. Mean curvature, $H = \frac{1}{2}(\kappa_1 + \kappa_2)$ and Gaussian curvature $K = \kappa_1 \kappa_2$ are both local geometry properties of the surface which reveal the local topology characters. We propose a method that directly computes the curvature information from either depth images and use the information to help further sampling. We used mean curvature in our experiment thus we only describe the detail for mean curvature only, for Gaussian curvature please refer to our supplementary material.

We suggest utilizing depth information to compute Gaussian and mean curvatures during initial voxel volume using depth, as described in the work of Sommer et al. [24]. This information can be employed for subsequent sampling. Depth can be viewed as a Monge patch of a surface, i.e. $z = D(x, y), (x, y) \in \Omega \subset \mathbb{R}^2$, where D is depth image and pixel coordinates (x, y) lay in image domain Ω [8; 25], which allows for the computation of these curvatures. Thus, the Monge patch $\mathcal{M} : \Omega \rightarrow \mathbb{R}^3$ is

$$\mathcal{M}(x, y) = (x, y, D(x, y)). \quad (5)$$

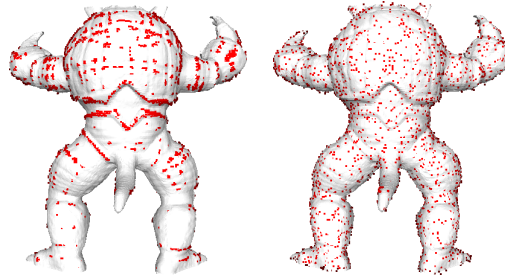


Figure 2: points gathering on high curvature effect (left) and our sampling results after considering points mean curvature (right).

To compute the two types of curvature from the depth

$$K(x, y) = \frac{D_{xx}D_{yy} - D_{xy}^2}{(1 + D_x + D_y)^2}, \quad (6)$$

$$H(x, y) = \frac{(1 + D_x^2)D_{yy} - 2D_xD_yD_{xy} + (1 + D_y^2)D_{xx}}{2(1 + D_x^2 + D_y^2)^{3/2}}, \quad (7)$$

where $D_x = \frac{\partial D(x,y)}{\partial x}$ is the partial derivatives of depth w.r.t x -axis in image plan, similarly, $D_y = \frac{\partial D(x,y)}{\partial y}$, $D_{xy} = \frac{\partial^2 D(x,y)}{\partial x \partial y}$, same for D_{xx} and D_{yy} . Depth, as a local representation of the surface in the form of a Monge patch, is dependent on a specific coordinate system. In order to compute the curvature for each voxel, it is necessary to integrate the separately calculated curvatures into a single voxel. Fortunately, both mean curvature and Gaussian curvature are local properties that remain invariant under changes in the coordinate system. In fact, according to [8; 25], we have the following lemma

Lemma *Mean curvature $H(x, y)$ and Gaussian curvature $K(x, y)$ are invariant to changes in the parameterization of the smooth surface represented by $\mathcal{M}(x, y) \in \mathbb{R}^3$ where $(x, y) \in \Omega \subset \mathbb{R}^2$ as long as the Jacobian of the parameter transformation is non-zero.*

We need to prove that the transformation between depth image coordinates has non-zero Jacobian. The proof is provided in the supplementary material. In a real application, a lot of objects especially large scenes are not closed for a small portion of the area. Or due to the visibility issues, one can not recover the unseen part without further processing. To address the problem of SDF that is mentioned in section 2, we propose to use a weight-aware SDF to create a pseudo-SDF by defining an artificial inside and outside criterion for an unclosed surface. The idea is, for the unclosed area, we see it as a degenerated patch while extracting surfaces using the marching cubes algorithm. In the classical SDF methods [24; 16], weights are widely used to integrate depth values into a voxel cube, the weights of each computed distance value indicate how reliable the value is. Another advantage of adding weight is that, for point cloud or gradient-SDF voxel input, the ground truth information is missing when sampling outside of surface points, setting the weight to zero can eliminate the artifacts caused by outside sampling.

4.3 Degenerated Local Surface Area

Mathematically, a degenerate surface refers to a surface that has singular points or when collapse happens. A singular point is a point on the surface where the surface is not smooth and fails to have a well-defined tangent plane. Degeneracies refer to situations where the surface degenerates into a simpler form, such as a line or a point. For example, a triangle can shrink to a line or a point if one or two vertices collapse to the other. For the unclosed area, we use the weight to indicate whether the vertice lies on a degenerated facet or not. If the facet is degenerated, that means the surrounding area of the vertices is collapsed to a point. To extract the surface using Marching cubes with weight, we propose to use weighted-marching cubes which can reconstruct the mesh of an unclosed surface, as shown in Figure 3, where a normal, and two degenerated situations when extracting triangles are visualized. In the normal case, the red voxel has a negative SDF value while values of other voxels are positive, when all voxels are valid, i.e. with positive weight, then we can determine the surface within this voxel cube. When some voxels have zero weight (black points), that means degeneracy happens inside this cube, the triangle facet collapse either to a line or a point. Thus, the unclosed surface is represented as a weight-aware neural signed distance function.

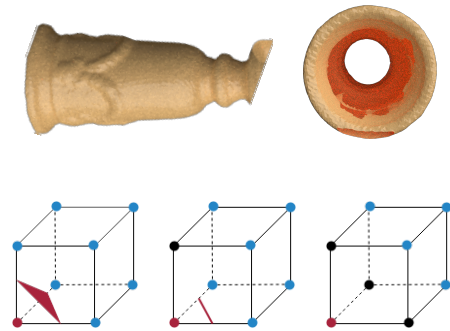


Figure 3: Unclosed surface visualization. The first row is a vase with an empty inside part. The second row shows how triangles in weighted marching cubes are degenerated.

4.4 Weight-Aware Signed Distance Field

To determine the weight of each sampled point. If the voxel volume is initialized using depth, then the weight of each voxel is computed using gradient-SDF [24], thus the sampled point \mathbf{x} inherits the voxel $\mathbf{v}(\mathbf{x})$ weight w^v . The weight allows us to sample far away from the surface. In equation (2), ψ^x is determined by Taylor expansion but the value only makes sense if the voxel $\mathbf{v}(\mathbf{x})$ contains a surface point, otherwise, the ψ^v will be the initial value. Luckily, if the voxel does not contain a surface point, its weight w^v is by design 0, thus, the sampled point \mathbf{x} weight is also 0 as described in section 4.

Remark We present our method based on depth input, however, our method can smoothly extend to the point cloud and normal input by voxelized the point cloud and computing curvature information in a voxel grid. For the details and more results please refer to our supplementary material.

5 Weight-Aware Neural Presentation of Surface

Given a set of noisy depth map $\mathcal{D} = \{D_k(x, y)\} \subset \mathbb{R}^2$ of an underlying surface \mathcal{S} , we first construct its voxel volume $\{\mathbf{v}_i\} \subset \mathbb{R}^3$ which contains its signed distance value $\psi^v \in \mathbb{R}$, gradient $\mathbf{g}^v \in \mathbb{R}^3$, weight $w^v \in \mathbb{R}$ and mean curvature information $k^v \in \mathbb{R}$, which are computed using (7). We would like to recover the neural implicit function $f : \mathbb{R}^3 \rightarrow \mathbb{R}$, and a weight function $\rho : \mathbb{R}^3 \rightarrow [0, 1]$ such that

$$f(\mathbf{x}, \theta) = d_{\mathcal{S}}(\mathbf{x}), \quad \text{for } |d_{\mathcal{S}}(\mathbf{x})| = \min_{\mathbf{y} \in \mathcal{S}} \|\mathbf{x} - \mathbf{y}\|, \quad (8)$$

$$\rho(\mathbf{x}, \theta_r) = \begin{cases} 1 & \text{if } \mathbf{x} \text{ is on non-degenerated area,} \\ 0 & \text{otherwise.} \end{cases} \quad (9)$$

$d_{\mathcal{S}}(\mathbf{x})$ is the signed distance of the point \mathbf{x} to the target surface \mathcal{S} which we want to predict. Given a point \mathbf{x} in the sample domain $\Gamma \subset \mathbb{R}^3$, as described in section 4 assume point \mathbf{x} falls in voxel $\mathbf{v}(\mathbf{x})$ with weight w^v , according to equation (2), we have the loss function of geometric constraint and normal constraint is

$$l_{\mathcal{X}}(\theta) = \frac{1}{|\Gamma^+|} \int_{\Gamma^+} (|f(\mathbf{x}, \theta) - \psi^v - \mathbf{g}^{\top}(\mathbf{v}(\mathbf{x}) - \mathbf{x})|) d\Gamma, \quad (10)$$

$$l_{\mathcal{N}}(\theta) = \frac{1}{|\Gamma^+|} \int_{\Gamma^+} (1 - \langle \frac{\nabla f(\mathbf{x}, \theta)}{\|\nabla f(\mathbf{x}, \theta)\|}, \hat{\mathbf{g}} \rangle) d\Gamma. \quad (11)$$

where Γ^+ indicate the area where sampled weight $w > 0$. The term (11) evaluates the cosine similarity of surface normal and implicit function gradient. Moreover for weight function ρ , we have

$$l_{\mathcal{W}}(\theta_r) = \int_{\Gamma} |\rho(\mathbf{x}, \theta_r) - w^v| d\Gamma. \quad (12)$$

The final loss

$$l(\theta, \theta_r) = l_{\mathcal{X}}(\theta) + \tau_n l_{\mathcal{N}}(\theta) + \tau_w l_{\mathcal{W}}(\theta_r) + \tau_e l_{\mathcal{E}}(\theta). \quad (13)$$

Curvature-guided sampling As mentioned in the previous sections, the mean curvature information is computed and cached into voxels. To avoid the uneven sampling problem which is mentioned in section 2, we divide these voxels into low, median, and high curvature voxels, similar to the work [17], instead, we use the mean curvature. For each epoch, we sample $2m$ points, where m from the surface points equally from the three curvature categories, i.e. for points we get from equation (3), are sampled from low curvature category $\hat{\mathbf{x}} \sim \{\mathbf{x} \in \Gamma \mid k < \underline{k}\}$, median curvature category $\hat{\mathbf{x}} \sim \{\mathbf{x} \in \Gamma \mid \underline{k} \leq k < \bar{k}\}$, and high curvature category $\hat{\mathbf{x}} \sim \{\mathbf{x} \in \Gamma \mid k \geq \bar{k}\}$. The threshold \underline{k} and \bar{k} are chosen by the 0.2 and 0.9 percentile of the curvature range. The visualized sampling results are shown in Figure 2. We sample m points randomly in domain Γ in the space and use equation (2) to get the corresponding SDF value and use as described in section 4.1 to get the weight of the points.

6 Evaluation

To demonstrate the effectiveness of our sampling method in improving the robustness and accuracy of the original surface reconstruction method, as well as extending its applicability to unclosed objects

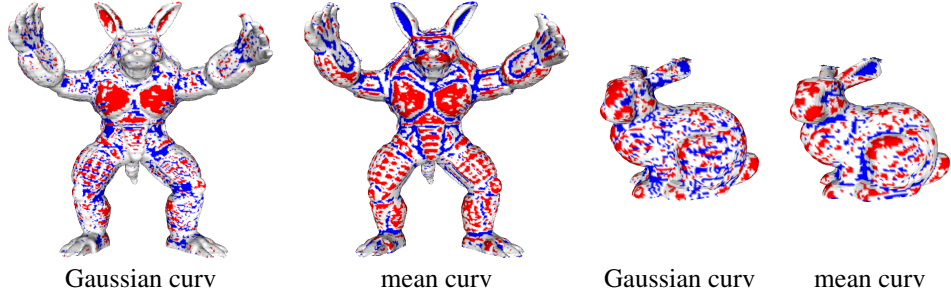


Figure 4: The visualization of Gaussian curvatures and mean curvatures of each point using the method that is described in section 4.2.

such as scenes, we evaluate our approach on both synthetic and real-world datasets, covering closed surfaces and scenes. We adopt SIREN [23] and MLP network (IGR [11]) as our base architecture and apply our sampling method and loss function as detailed in section 5 to showcase that our sampling method improves the accuracy without changing network architectures. Here we only visualize the result from the SIREN network, for more results please see our supplementary material. For the SIREN network, we use 8 SIREN layers with 256 nodes for implicit signed distance prediction and a 5 SIREN layer network with the same node number as the implicit network for weight prediction. To test the improvement on IGR [11] we use an 8-layer MLP with 512 nodes and a 5 MLP layer for SDF and weight prediction respectively. We set the learning rate at 10^{-4} with decay and use mean curvature for curvature-guided sampling, the batch size is $10k$ and we train $10k$ epochs for each dataset. Our PyTorch implementation takes approximately 2 hour to train on a GeForce GTX TITAN X GPU with CUDA for each dataset. The evaluation consists of three parts: 1) quantitative assessment of synthetic object reconstruction, 2) qualitative evaluation of real-world object and scene reconstruction, and 3) qualitative comparison of curvature-guided sampling and uniform sampling methods.

6.1 Differentiable Curvature of Surface

We visualize mesh points with low, median, and high mean curvature, as calculated according to subsection 4.2, equations (7) and demonstrates that the curvature derived by our method corresponds to the local geometric features of the surface area. The red color indicates a high curvature area and the blue color indicates a low curvature area. A positive mean curvature ($H > 0$) signifies a convex surface, while a negative mean curvature ($H < 0$) indicates a concave surface. Positive Gaussian curvature ($K > 0$) indicates that the surface is locally shaped like a dome or sphere at that point, and negative Gaussian curvature ($K < 0$) indicates that the surface is locally saddle-shaped or hyperbolic at that point. Figure 4 displays that the computed curvature indeed captures the local geometric properties of the surface.

6.2 Surface Reconstruction Results

We evaluate our method on four types of datasets: synthetic object datasets [7] featuring noiseless, smooth meshes; real-world object datasets [27] with only RGB images, depth images, and camera poses available; synthetic scene datasets [12] containing RGB images, noiseless depth images, and ground truth poses; and finally, real-world scene datasets [5] providing solely RGB and depth images. We will demonstrate that our method performs well across all types of datasets and is capable of handling both object and scene reconstruction tasks.

For the synthetic scene, object, and real-world object datasets, we fuse depth images into a voxel grid with 256 resolution based on the given poses and compute curvature information from depth images simultaneously. The depth images for synthetic objects are generated using Blender software. For the real-world scene dataset [5], poses are estimated additionally while fusing depth images. Subsequently, the input point cloud is extracted from the voxel grid to train IGR [11] and SIREN [23], as well as for the proposed method for sampling on the surface. The works of Chibane et al. [3; 4] need mesh as input therefore the ground truth mesh is used.

Figure 5 qualitatively demonstrates the robustness of our method across synthetic and real-world datasets. Synthetic datasets typically contain convex and closed surfaces (except at the bottom), while real-world datasets may have concave parts and noisy point clouds due to inaccurate camera poses or noisy depth images, leading to failure cases.

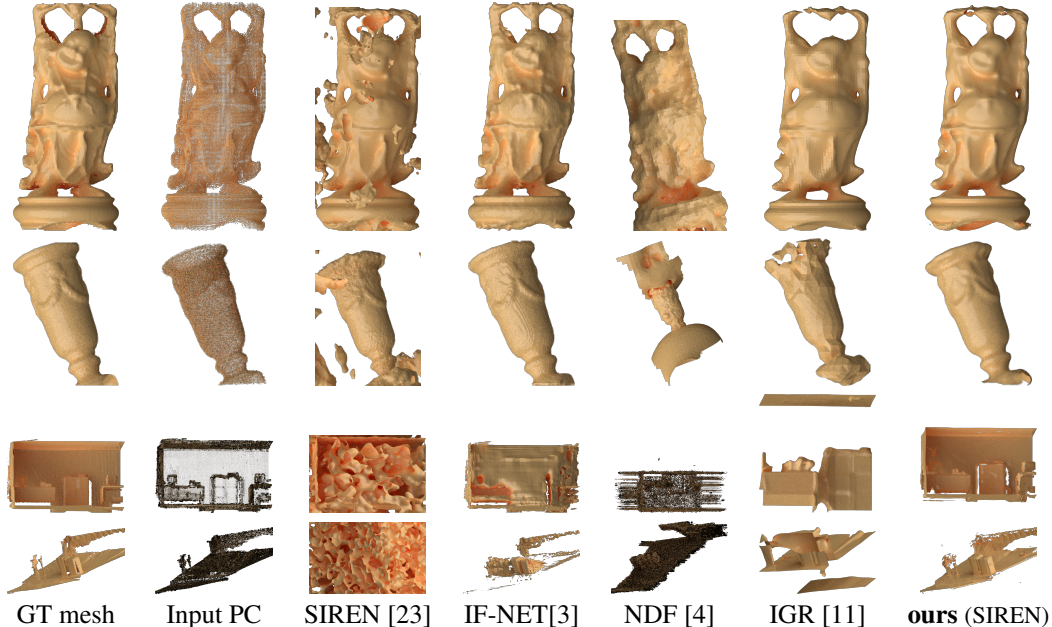


Figure 5: The visualization of the reconstructed mesh of our method and baseline methods. The first two rows are the visualization of the synthetic (*happy buddha* and real-world data (*vase*)). The mesh is generated using 128 resolution voxel grid. The real-world dataset is much noisier, especially around the top of the vase thus it is more challenging. The third and fourth rows are the results of a synthetic scene *of_kt0* and a real-world scene from the *Redwood* dataset [5]. The meshes are generated by a grid with 256 resolution.

For synthetic object datasets where ground truth is available, we compute quantitative errors, including Chamfer Distance (CD) [13], Hausdorff Distance (HD) [20], and Earth Mover’s Distance (EMD)[21; 6; 19].

SIREN experiences significant errors, primarily due to noise outside the reconstruction. NDF [3] outputs a denser point cloud, and we recover the mesh using the Ball-Pivoting Algorithm (BPA)[1] following the authors’ instructions. IF-NET[3] exhibits visually pleasing results but suffers from high error rates due to surface noise and artifacts caused by voxelization.

Finally, we evaluate our method on the open scenes dataset, namely *ICL-NUIM* [12] and *Redwood* [5]. The results, shown in the last two rows of Figure 5, show that SIREN [23] struggles with the noise outside of the surface, especially in open real-world scenes. Surprisingly, NDF [4] fails possibly due to limited training data. IF-NET [3] and IGR [11], both requiring watertight mesh for input training data, can’t handle open scenes.

6.3 Random Sampling vs. Curvature-Guided Sampling

To demonstrate that curvature-guided sampling indeed improves the results, we did the ablation studies on the synthetic object datasets. We use uniform sampling and curvature-guided sampling respectively to sample m points as described in section 5. For each dataset, we train 500 epochs, and for every 5 epochs, we reconstruct the mesh to compute the Chamfer error, Hausdorff error, and EMD. The value is shown in last two columns of Table 1. For better visualization, we plot the Chamfer distance in Figure 7. The y-axis is the CD value and the number is normalized by dividing the biggest CD for each dataset. The solid line is the result of using curvature-guided sampling, the dashed line is random sampling. For all datasets except *bunny*, curvature-guided sampling leads to a faster reduction of the Chamfer error during training and reaches a smaller error after 500 epochs. For *bunny*, both sampling methods do not show much difference. A possible reason is that *bunny* has a simple and convex geometry, the curvature would not help as much as for a more complex shape such as *happy_buddha* (red lines) and *armadillo* (yellow line). The value in Table 1 also shows that for a complex object, the curvature-guided sampling significantly improved all three errors.

7 Conclusion

| Metric | Dataset | Method | | | | | | Ablation Study | |
|--------|--------------|----------|------------|----------|--------------|--------------|--------------|----------------|-----------------|
| | | NDF [4] | SIREN [23] | IGR [11] | IF-NET [3] | OURS (SIREN) | OURS (MLP) | OURS (curv) | OURS (w/o curv) |
| CD | Armadillo | 5148.128 | 3990.748 | 1.484 | 0.634 | 0.704 | 1.146 | 1.952 | 0.704 |
| | Bunny | 2828.111 | 256.120 | 37.210 | 24.427 | 23.265 | 4.052 | 23.265 | 24.879 |
| | Happy Buddha | 2376.664 | 1607.579 | 8.182 | 10.216 | 10.216 | 2.015 | 3.414 | 3.348 |
| | Dragon | 1233.421 | 2079.948 | 15.638 | 12.815 | 12.815 | 1.403 | 2.854 | 2.137 |
| | Average | 2896.581 | 1983.599 | 15.628 | 12.023 | 6.847 | 3.106 | 7.871 | 7.767 |
| HD | Armadillo | 235.919 | 195.757 | 0.709 | 0.321 | 0.348 | 0.693 | 1.702 | 0.348 |
| | Bunny | 176.381 | 165.235 | 12.915 | 9.545 | 11.889 | 2.877 | 10.533 | 11.753 |
| | Happy Buddha | 246.161 | 165.173 | 6.584 | 3.749 | 3.749 | 1.139 | 2.030 | 2.297 |
| | Dragon | 84.829 | 144.412 | 4.535 | 5.227 | 5.227 | 0.825 | 1.649 | 0.825 |
| | Average | 185.822 | 167.644 | 6.186 | 4.711 | 3.550 | 2.002 | 3.978 | 3.806 |
| EMD | Armadillo | 18.999 | 465.363 | 7.139 | 2.648 | 0.538 | 0.139 | 0.301 | 0.538 |
| | Bunny | 78.204 | 30.645 | 22.866 | 30.970 | 30.970 | 1.350 | 1.459 | 1.350 |
| | Happy Buddha | 94.071 | 37.590 | 20.986 | 27.613 | 27.613 | 5.130 | 7.548 | 5.819 |
| | Dragon | 173.817 | 80.234 | 11.319 | 13.215 | 13.215 | 0.149 | 2.015 | 0.149 |
| | Average | 91.273 | 153.458 | 15.577 | 18.612 | 18.612 | 1.792 | 2.831 | 1.964 |

Table 1: A comparison of our method with other baseline approaches for implicit neural surface reconstruction. For each synthetic object dataset, we show Chamfer Distance (CD), Hausdorff Distance (HD), and Earth Move’s Distance (EMD), averaging over 50000 points. The CD, HD, EMD results in the table are scaled by a factor of 10^4 , 10^2 , and 10^3 respectively for the readability. The last two columns of the method part are the results of two different underlying network architectures using our sampling method and loss function. The numbers show that our sampling method enhances reconstruction accuracy in both cases.

Conclusion In this work, we have presented a novel weight-aware implicit surface representation to broaden the signed distance field applicability to non-enclosed objects and environments. We also propose a sampling method that uses hybrid representation: voxel and point cloud for easily interpolating and extrapolating data for neural implicit learning. Our proposed technique effectively enhances the performance of baseline methods without necessitating changes to the network architecture. Through evaluations conducted on synthetic and real-world datasets encompassing both closed surfaces and scenes, our method exhibits commendable results in the reconstruction of both enclosed objects and open scenes. Furthermore, the ablation study on curvature-guided sampling substantiates the improvement in the accuracy and efficiency of training the model.

Limitations Our approach does not specialize in surface completion; hence, it fails to recover any missing areas in the input point cloud or depth data, implying its inability to handle occlusion.

Future Work The techniques presented in this work can be easily integrated with other neural reconstruction methods and shape completion techniques. Moving forward, our plan is to incorporate shape completion and neural rendering techniques to deal with missing areas.

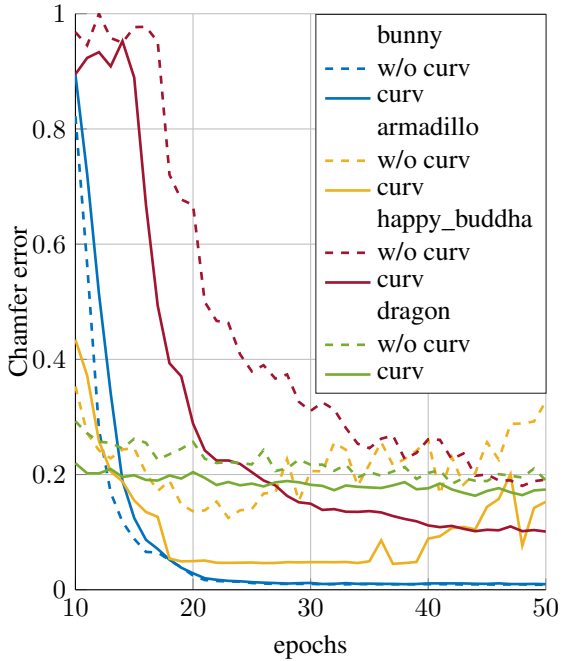


Figure 6: Chamfer distance curve for different sampling methods in four synthetic datasets. Dashed line is uniform-sampling and solid line is curvature-guided sampling. All datasets expect bunny, the curvature-guided sampling indeed achieves smaller error faster.

References

- [1] F. Bernardini, J. Mittleman, H. Rushmeier, C. Silva, and G. Taubin. The ball-pivoting algorithm for surface reconstruction. *IEEE Transactions on Visualization and Computer Graphics*, 5(4):349–359, 1999.
- [2] Z. Chen and H. Zhang. Learning implicit fields for generative shape modeling. In *2019 IEEE/CVF Conference on Computer Vision and Pattern Recognition (CVPR)*, pages 5932–5941, 2019.
- [3] J. Chibane, T. Alldieck, and G. Pons-Moll. Implicit functions in feature space for 3d shape reconstruction and completion. *CoRR*, abs/2003.01456, 2020.
- [4] J. Chibane, A. Mir, and G. Pons-Moll. Neural unsigned distance fields for implicit function learning. In *Advances in Neural Information Processing Systems (NeurIPS)*, December 2020.
- [5] S. Choi, Q.-Y. Zhou, S. Miller, and V. Koltun. A large dataset of object scans. *arXiv:1602.02481*, 2016.
- [6] S. Cohen, L. J. Guibas, and O. Sorkine-Hornung. Deep learning with point clouds and earth mover’s distance. 2019.
- [7] B. Curless and M. Levoy. A volumetric method for building complex models from range images. In *Proceedings of the 23rd Annual Conference on Computer Graphics and Interactive Techniques, SIGGRAPH ’96*, page 303–312, New York, NY, USA, 1996. Association for Computing Machinery. ISBN 0897917464. doi: 10.1145/237170.237269. URL <https://doi.org/10.1145/237170.237269>.
- [8] M. P. do Carmo. *Differential geometry of curves and surfaces*. Prentice Hall, 1976. ISBN 978-0-13-212589-5.
- [9] K. Genova, F. Cole, A. Sud, A. Sarna, and T. A. Funkhouser. Deep structured implicit functions. *ArXiv*, abs/1912.06126, 2019.
- [10] R. Goldman. Curvature formulas for implicit curves and surfaces. *Computer Aided Geometric Design*, 22(7):632–658, 2005. ISSN 0167-8396. doi: <https://doi.org/10.1016/j.cagd.2005.06.005>. URL <https://www.sciencedirect.com/science/article/pii/S0167839605000737>. Geometric Modelling and Differential Geometry.
- [11] A. Gropp, L. Yariv, N. Haim, M. Atzmon, and Y. Lipman. Implicit geometric regularization for learning shapes. *arXiv preprint arXiv:2002.10099*, 2020.
- [12] A. Handa, T. Whelan, J. McDonald, and A. Davison. A benchmark for RGB-D visual odometry, 3D reconstruction and SLAM. In *IEEE Intl. Conf. on Robotics and Automation, ICRA*, Hong Kong, China, May 2014.
- [13] L. Landrieu and M. Boussaha. Point cloud oversegmentation with graph-structured deep metric learning. *2019 IEEE/CVF Conference on Computer Vision and Pattern Recognition (CVPR)*, pages 7432–7441, 2019.
- [14] L. M. Mescheder, M. Oechsle, M. Niemeyer, S. Nowozin, and A. Geiger. Occupancy networks: Learning 3d reconstruction in function space. *CoRR*, abs/1812.03828, 2018.
- [15] M. Michalkiewicz, J. K. Pontes, D. Jack, M. Baktashmotlagh, and A. P. Eriksson. Deep level sets: Implicit surface representations for 3d shape inference. *CoRR*, abs/1901.06802, 2019.
- [16] R. A. Newcombe, S. Izadi, O. Hilliges, D. Molyneaux, D. Kim, A. J. Davison, P. Kohi, J. Shotton, S. Hodges, and A. Fitzgibbon. Kinectfusion: Real-time dense surface mapping and tracking. In *2011 10th IEEE international symposium on mixed and augmented reality*, pages 127–136. Ieee, 2011.
- [17] T. Novello, G. Schar Dong, L. Schirmer, V. da Silva, H. Lopes, and L. Velho. Exploring differential geometry in neural implicits, 2022.
- [18] J. J. Park, P. Florence, J. Straub, R. A. Newcombe, and S. Lovegrove. Deepsdf: Learning continuous signed distance functions for shape representation. *CoRR*, abs/1901.05103, 2019.
- [19] O. Pele and M. Werman. Fast and robust earth mover’s distances. In *2009 IEEE 12th International Conference on Computer Vision*, pages 460–467. IEEE, September 2009.
- [20] R. T. Rockafellar. Hausdorff distance in the space of closed subsets. *Pacific Journal of Mathematics*, 43(2): 555–568, 1972.
- [21] Y. Rubner, C. Tomasi, and L. J. Guibas. The earth mover’s distance as a metric for image retrieval. *International Journal of Computer Vision*, 40(2):99–121, 2000.

- [22] L. Sang, B. Haefner, X. Zuo, and D. Cremers. High-quality rgb-d reconstruction via multi-view uncalibrated photometric stereo and gradient-sdf. In *IEEE Winter Conference on Applications of Computer Vision (WACV)*, Hawaii, USA, January 2023.
- [23] V. Sitzmann, J. N. Martel, A. W. Bergman, D. B. Lindell, and G. Wetzstein. Implicit neural representations with periodic activation functions. In *Proc. NeurIPS*, 2020.
- [24] C. Sommer, L. Sang, D. Schubert, and D. Cremers. Gradient-SDF: A semi-implicit surface representation for 3d reconstruction. In *IEEE Conference on Computer Vision and Pattern Recognition (CVPR)*, 2022.
- [25] M. Spivak. *A Comprehensive Introduction to Differential Geometry*. Number Bd. 1 in A Comprehensive Introduction to Differential Geometry. Publish or Perish, Incorporated, 1999. ISBN 9780914098706. URL <https://books.google.de/books?id=ahSWQgAACAAJ>.
- [26] G. Yang, S. Belongie, B. Hariharan, and V. Koltun. Geometry processing with neural fields. In *Thirty-Fifth Conference on Neural Information Processing Systems*, 2021.
- [27] M. Zollhöfer, A. Dai, M. Innmann, C. Wu, M. Stamminger, C. Theobalt, and M. Nießner. Shading-based refinement on volumetric signed distance functions. *ACM Transactions on Graphics (TOG)*, 34(4):1–14, 2015.

A1 Code, Datasets, and baseline methods

Our code and evaluation scripts will be publicly available soon. We will also provide detailed information about the code of baseline methods as well as the evaluation script for reproducibility.

| | name | type | year | link | license |
|------|--------------------|---------|------|---|-----------------|
| [5] | Redwood | dataset | 2016 | http://www.redwood-data.org/3dscan/ | Public Domain |
| [7] | The Stanford 3D | dataset | 1994 | http://graphics.stanford.edu/data/3Dscanrep/ | Public Domain |
| [27] | multi-view dataset | dataset | 2015 | http://graphics.stanford.edu/projects/vsfs/ | CC BY-NC-SA 4.0 |
| [12] | ICL-NUIM | dataset | 2014 | https://www.doc.ic.ac.uk/~ahanda/VaFRIC/iclnuim.html | CC BY 3.0 |
| [24] | gradient-SDF | code | 2022 | https://github.com/c-sommer/gradient-sdf | BSD-3 |
| [11] | IGR | code | 2020 | https://github.com/amosgropp/IGR | - |
| [23] | SIREN | code | 2019 | https://github.com/vsitzmann/siren | MIT license |
| [3] | IF-NETS | code | 2020 | https://virtualhumans.mpi-inf.mpg.de/ifnets/ | - |
| [4] | NDF | code | 2020 | https://virtualhumans.mpi-inf.mpg.de/ndf/ | - |

Table A.3: Used datasets and code in our submission, together with reference, link, and license. We did our real-world experiments on two datasets, multi-view dataset [27] (for which ground truth poses exist), and Redwood LOD (without ground truth poses). Two synthetic dataset, the Stanford 3D [7], which is an object dataset, and ICL-NUIM dataset [12], which is a scene dataset. For the comparison methods, we use the code listed in the table.

A2 Mathematical detail

| Symbol | Description | Symbol | Description |
|---------------------------------------|--|--|--|
| $\mathbf{x} \in \mathbb{R}^3$ | 3D points | $\mathcal{P} \subset \mathbb{R}^3$ | point cloud set |
| $\mathcal{V} \subset \mathbb{N}^+$ | points index set | $\mathcal{S} \subset \mathbb{R}^3$ | continuous surface |
| $f(\mathbf{x}, \theta)$ | neural implicit function | $\theta \in \mathbb{R}^{n \times m}$ | learnable parameter |
| $\rho(\mathbf{x}, \theta_r)$ | weight function | $\theta_r \in \mathbb{R}^{n \times m}$ | learnable parameter of weight function |
| $\psi^v \in \mathbb{R}$ | voxel SDF value | $\psi^x \in \mathbb{R}$ | point SDF value |
| $\hat{\mathbf{g}}^v \in \mathbb{R}^3$ | normalized distance gradient | $\mathbf{g}^v \in \mathbb{R}^3$ | voxel distance gradient |
| $w^v \in \mathbb{R}$ | voxel weight | $k \in \mathbb{R}$ | point curvature |
| $\Gamma \subset \mathbb{R}^3$ | sample domain | $\gamma \in \mathbb{R}$ | SDF threshold |
| $K \in \mathbb{R}$ | Gaussian curvature | $H \in \mathbb{R}$ | mean curvature |
| k_1, k_2 | principal curvature | $D \subset \mathbb{R}^2$ | depth image |
| $\Omega \subset \mathbb{R}^2$ | image domain | $\mathcal{M} \subset \mathbb{R}^3$ | Monge path |
| $d_S(\cdot)$ | signed distance to surface \mathcal{S} | $\Gamma^+ \subset \mathbb{R}^3$ | sample domain with positive weight |
| $\bar{k} \in \mathbb{R}$ | higher threshold | $\underline{k} \in \mathbb{R}$ | lower threshold of curvature |
| $F(\mathbf{x})$ | discrete implicit function | ∇ | differential operator |
| $\mathbf{n}_i \in \mathbb{R}^3$ | known points normal | $Q \in \mathbb{R}^{3 \times 3}$ | camera intrinsic matrix |
| $R \in SO(3)$ | camera rotation matrix | $\mathbf{t} \in \mathbb{R}^3$ | camera translation vector |

Table A.4: Summary of our notation in the main paper and in the supplementary material.

A2.1 Proof of the Proposition

In the paper Lemma of section 4.2, we mention that the transformation between two depth coordinates has non-zero Jacobian (non-zero determinant) hence the integration of curvatures from depth images makes sense. Here is the formulation and proof.

The determinant of the Jacobian of the parameter transformation of the parameterization in the two depth images is non-zero, thus the mean curvature $H(x, y)$ and Gaussian curvature $K(x, y)$ are invariant.

Proof Given two depth images D_1 and D_2 taken at 2 different positions. Suppose the transformation from position 1 to position 2 is a rigid body motion $T = [R, \mathbf{t}]$, where $R \in SO(3)$ is a rotation matrix and $\mathbf{t} \in \mathbb{R}^3$ is a translation vector. Let pixel $p = (x, y)$ in D_1 , $0 \neq z = D_1(x, y)$, and $Q \in \mathbb{R}^{3 \times 3}$ be the camera intrinsic matrix, then the transformation of pixel p to $\bar{p} = (\bar{x}, \bar{y})$ in D_2 is

$$\bar{z} \begin{bmatrix} \bar{x} \\ \bar{y} \\ 1 \end{bmatrix} = Q(R(Q^{-1} \begin{bmatrix} x \\ y \\ 1 \end{bmatrix})z + \mathbf{t}), \quad (14)$$

where

$$Q = \begin{bmatrix} f_x & 0 & c_x \\ 0 & f_y & c_y \\ 0 & 0 & 1 \end{bmatrix}$$

is invertible, f_x, f_y is the camera focal length and c_x, c_y is the principal points. The pixel 3D coordinates in under two camera view is $Q^{-1}(x, y, 1)^\top z$ and $Q^{-1}(\bar{x}, \bar{y}, 1)^\top \bar{z}$. Let $\{r_{ij}\}_{i,j} \in \{1, 2, 3\}$ be the element in R and $\mathbf{t} = (t_1, t_2, t_3)^\top$, compute the right side, we have $\bar{z} = r_{31}x + r_{32}y + r_{33}z + t_3$ is the depth value after a rigid body motion and $\bar{z} \neq 0$ since it does not fall to image plane of D_2 as we assume the point is visible in both camera position.

$$\det(QRQ^{-1}) = \det(Q) \det(R) \det(Q)^{-1} = 1, \quad (15)$$

it is because $\det(Q) \neq 0$, $\det(R) = 1$ and $\det(Q^{-1}) = \det(Q)^{-1}$. Thus the transformation Jacobian of the 3D points is non-zero. For the Jacobian of the transformation from (x, y) to (\bar{x}, \bar{y}) , we only need to consider the upper-left 2×2 submatrix of QRQ^{-1} . Since the upper-left 2×2 matrix of R represents the rotation matrix in xy plane, thus it is non-zero. The upper-left 2×2 matrix of Q is diagonal, also non-zero. Hence, we get the determinant of Jacobian from (x, y) to (\bar{x}, \bar{y}) is also non-zero.

A2.2 Voxlized Point Cloud and its Curvature

Point cloud voxelization Given a point cloud with normals $\mathcal{P} = \{\mathbf{x}_i, \mathbf{n}_i\}, i \in \mathcal{V}$. We construct a voxel grid of size $n \times n \times n$, with each voxel element of edge length s . The center of the i -th voxel is denoted as $\mathbf{v}_i \in \mathbb{R}^3$. Further, we align the given point cloud and constructed a voxel grid, such that their central points are both located in the origin. Then the distance value of \mathbf{v}_i to the surface can be found by the nearest neighbor search to the closest surface point. The sign is determined by the angle of the direction from the voxel center to the surface point and the normal of the surface point, i.e. the signed distance of voxel \mathbf{v}_i is

$$\psi_i^v = \min_{k \in \mathcal{V}} \mathbf{n}_k^\top \|\mathbf{v}_i - \mathbf{x}_k\| \quad (16)$$

To initialize the weight, we assign the weight for each voxel to 1 if the voxel contains a surface point, otherwise, the weight is assigned to zero. That is, for voxel with edge length s ,

$$w^v = \begin{cases} 1, & |\psi^v| < \sqrt{3}s, \\ 0, & \text{otherwise.} \end{cases} \quad (17)$$

$\sqrt{3}s$ is the diagonal length of a voxel element, which is the largest distance inside a voxel. In the sampling procedure, weight allows us to sample far away from the surface. Moreover, we also assign $\hat{\mathbf{g}}^v = \mathbf{n}$ for voxel with positive weight as they are close enough to the surface and using the fact that distance gradient and surface normal coincide near the iso-surface. Now for voxel set $\{\mathbf{v}_i\}$, we have voxel \mathbf{v} together with its weight w^v , signed distance ψ^v , and gradient $\hat{\mathbf{g}}^v$, if its weight is positive. The next step is to compute the curvature information.

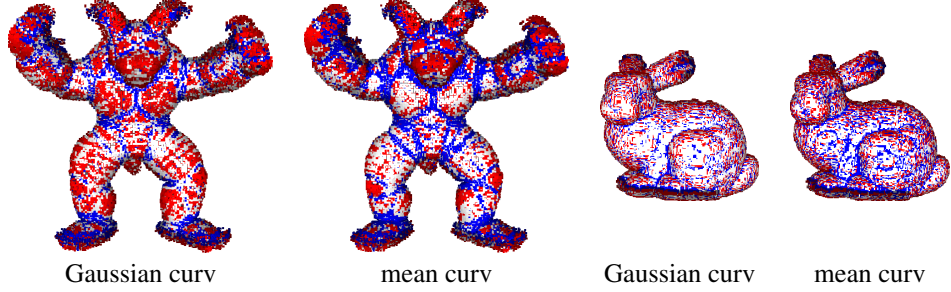


Figure A.7: The visualization of Gaussian curvatures and mean curvatures of each point using the voxelized voxel grid.

Curvature from implicit function The voxel grid is initialized from a point cloud, denoting the discrete implicit SDF function as $F : \mathbb{R}^3 \rightarrow \mathbb{R}$, e.g. $F(\mathbf{v}_i) = \psi_i^v$.

Then, for point \mathbf{x} on the iso-surface, that is $F(\mathbf{x}) = 0$, we have [10]

$$K(\mathbf{x}) = \frac{\nabla F(\mathbf{x}) \nabla^{2*}(\mathbf{x}) \nabla F(\mathbf{x})^\top}{|\nabla F(\mathbf{x})|^4} \quad (18)$$

$$H(\mathbf{x}) = \frac{\nabla F(\mathbf{x}) \nabla^2(\mathbf{x}) \nabla F(\mathbf{x})^\top - |\nabla F(\mathbf{x})|^2 \text{Tr}(\nabla^2(\mathbf{x}))}{2|\nabla F(\mathbf{x})|^3} \quad (19)$$

Where $\nabla^2 F(\mathbf{x})$ is the Hessian of implicit function F and $\nabla^{2*} F(\mathbf{x})$ is its adjoint. In the real computation, we use the divergence formula of Gaussian curvature

$$H(\mathbf{x}) = -\nabla \cdot \left(\frac{\nabla F(\mathbf{x})}{|\nabla F(\mathbf{x})|} \right) \quad (20)$$

The adjoint of Hessian is computed using

$$\nabla^{2*} F(\mathbf{x}) = \begin{pmatrix} F_{yy}F_{zz} - F_{yz}F_{zy} & F_{yz}F_{zx} - F_{yz}F_{zz} & F_{yx}F_{zy} - F_{yy}F_{zx} \\ F_{xz}F_{zy} - F_{xy}F_{zz} & F_{xx}F_{zz} - F_{xz}F_{zx} & F_{xy}F_{zx} - F_{zz}F_{zy} \\ F_{xy}F_{yz} - F_{xz}F_{yy} & F_{yz}F_{xz} - F_{xx}F_{yz} & F_{xx}F_{yy} - F_{xy}F_{yx} \end{pmatrix} \quad (21)$$

Visualization of curvature from implicit function To demonstrate our work can extend to point cloud input, we voxelize two point clouds and compute their SDF value using equation (16) and compute the Gaussian and mean curvature information as described in equation (18) and (19), see Figure A.7, we colored the points with high curvature in red and low curvature in blue.

Remark *Given that curvature is calculated using the discrete implicit function, differentiation is performed through the finite difference method. This method is contingent upon voxel size and voxelization accuracy, potentially leading to more inconsistent outcomes. In response to this issue, we suggest direct computation from depth images. This approach circumvents the reliance on discretization, thereby providing a more stable and smoother result.*

Visualization of point cloud input reconstruction Using the voxelization procedure mentioned before, we can still use our sampling method to recover the implicit neural function. We show the input point cloud, the recovered mesh directly after the voxelization and the result after training, see Figure A.8.

A3 More Quantitative Results

A3.1 Curvature Visualization

We also present visualizations of mean and Gaussian curvatures for two additional synthetic datasets that we have initialized using depth images. It’s important to note that Gaussian and mean curvature values can sometimes vary as they represent distinct geometric characteristics.

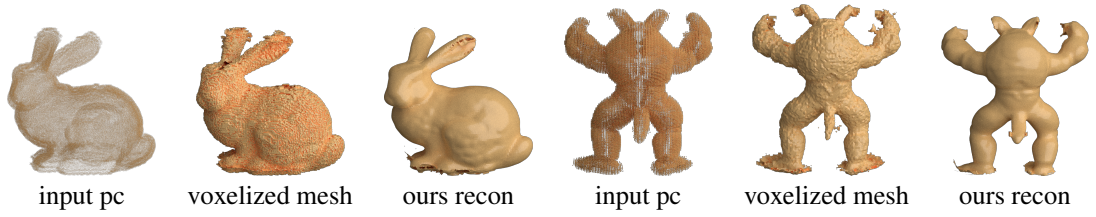


Figure A.8: The visualization results of input point cloud, the mesh generated directly after voxelization and the mesh generated by neural implicit function that is trained using proposed sampling method.

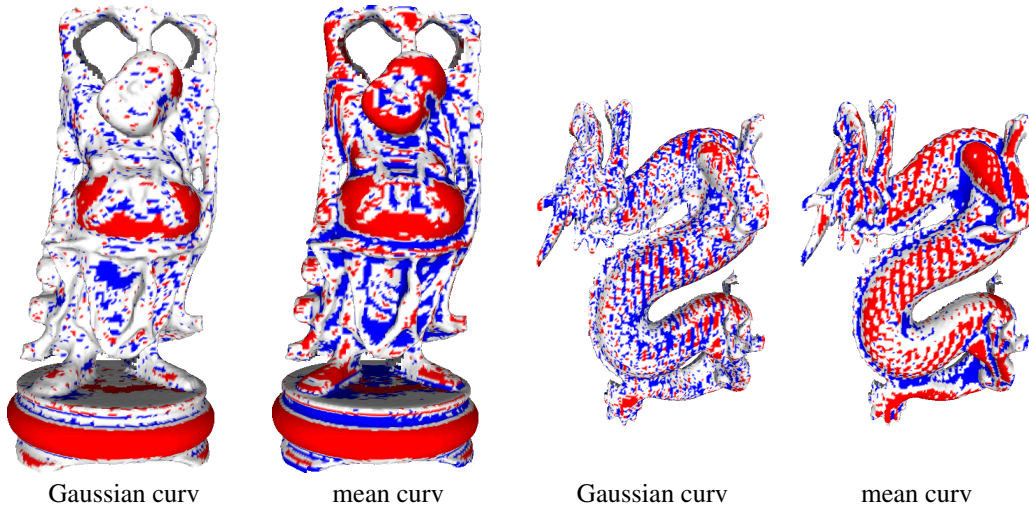


Figure A.9: The visualization of Gaussian curvatures and mean curvatures of *happy_buddha* and *dragon* dataset, computed using depth images as described in main paper section 4.2.

A3.2 Reconstruction Visualization Results

More visualization result of real world and synthetic datasets. The proposed method gives satisfactory results in different datasets while comparison results are either good for object synthetic datasets but fail for real-world datasets.



Figure A.10: More visualization results for both real-world (row 4 and row 7-8) and synthetic dataset (row 1-3 and row 5-6), include objects (row 1-4) and scene (row 5-8), additionally we also visualize our sampling and weight-aware method in SIREN network (i.e. SIREN [23]) as well as MLP network (i.e. IGR [11]).